Gordon Paul
School of Engineering and Materials Science,
Queen Mary University of London,
London E1 4NS, UK

Amin Rezaienia
School of Engineering and Materials Science,
Queen Mary University of London,
London E1 4NS, UK

Eldad Avital
School of Engineering and Materials Science,
Queen Mary University of London,
London E1 4NS, UK

Theodosios Korakianitis[1]
Professor
Parks College of Engineering,
Aviation and Technology,
Saint Louis University,
St. Louis, MO 63103
e-mail: korakianitis@alum.mit.edu

Machinability and Optimization of Shrouded Centrifugal Impellers for Implantable Blood Pumps

This paper describes the use of analytical methods to determine machinable centrifugal impeller geometries and the use of computational fluid dynamics (CFD) for predicting the impeller performance. An analytical scheme is described to determine the machinable geometries for a shrouded centrifugal impeller with blades composed of equiangular spirals. The scheme is used to determine the maximum machinable blade angles for impellers with three to nine blades in a case study. Computational fluid dynamics is then used to analyze all the machinable geometries and determine the optimal blade number and angle based on measures of efficiency and rotor speed. The effect of tip width on rotor speed and efficiency is also examined. It is found that, for our case study, a six- or seven-bladed impeller with a low blade angle provides maximum efficiency and minimum rotor speed. [DOI: 10.1115/1.4036287]

1 Introduction

Congestive heart failure (CHF) is one of the leading causes of death in Western countries. More than 7 million people in North America and Europe are diagnosed with heart failure, among whom nearly 6% are categorized as having New York Heart Association class IV heart failure [1]. As a result, the role of mechanical circulatory support (MCS) devices as a bridge to transplantation and as destination therapy has become vital for patients on and off the waiting list [2,3]. While the first blood pumps were membrane-based positive displacement devices, rotary blood pumps are prevalent in current clinical use.

The challenge for engineers is to build rotary blood pumps which are sufficiently small, generate the pressure and flow required by the patients, and are cost-effective to manufacture. These devices must generate the required hydraulic operating condition to support the target patient population, while exhibiting high efficiency in order to minimize the power loss and consequently minimize the volume and weight of the batteries carried by sick patients. The rotor speed must also be minimized to reduce the shear on blood in the secondary flow clearances and improve hemocompatibility.

This paper looks specifically at centrifugal impellers in rotary blood pumps. Examples of centrifugal impellers in implantable blood pumps include Heartmate III [4], HVAD [5], Duraheart [6], EvaHeart [7], and MiniVAD [8]. Of these, HVAD and Evaheart are commercially available, the former worldwide and the latter in the EU and Japan. Heartmate III and Duraheart use shrouded, 2D-extruded blade geometries. Evaheart, Heartmate III, and Duraheart use four, five, and six blades, respectively, which are curved, while HVAD and miniVAD use four and >12 blades, respectively, which are almost flat.

There are severe material constraints in manufacturing implantable blood pumps. The requirement for long-term hemocompatibility means that impellers are composed of as few different materials and pieces as possible, which are often welded together [9]. Rotors are nearly always fabricated by machining blades from a titanium alloy [10]. A shrouded impeller can be created by machining blades and shroud as separate pieces and welding them together but this requires complex processes to attach blade geometries in a seamless weld that does not encourage blood trauma. This increases manufacturing cost and complexity. Machining a shrouded impeller from a single piece is preferable.

This paper describes a methodology to find optimal geometries for shrouded impellers that can be machined from a single piece. An analytical scheme is used to determine whether an impeller is machinable. Computational fluid dynamics (CFD) analysis is then used to find the optimal geometries to maximize the efficiency and minimize rotor speed for all machinable designs. A case study is presented to demonstrate the methodology.

2 Background

The optimization of impellers for blood pumps has been presented by several groups [11–13]. Several objectives have been used for optimization, including efficiency, shear stress, and normalized index of hemolysis. An "optimal" blade design is different depending on which objectives are used and what other flow paths are associated with the blades. Here, CFD analysis is used to find both efficiency and rotor speed, which is used as an indicator of hemolysis. Efficiency is defined in this paper as the hydraulic output power as a percentage of the shaft input power. The previous work by our group has described the effect of blade angle and blade number on the efficiency and hydraulic performance of an impeller without secondary flow clearances [14]. This work combines the impeller hydraulic performance analysis with impeller manufacturability constraints for centrifugal blood pumps, modeling all hydraulic parts of the pump with CFD.

The geometric parameters in the design of a centrifugal impeller are the diameters of the hub and rim, blade thickness, outlet width, number of blades, and blade curvature. The blade curvature in particular has a significant effect on both machinability and hydraulic performance [15,16]. Higher blade curvature makes an impeller difficult to machine and increases the rotor speed required to reach the operating condition, but increases efficiency. A lower blade curvature is easier to machine and decreases the rotor speed required to reach the operating condition, but decreases efficiency. Increasing blade curvature increases the

[1]Corresponding author.

Manuscript received June 29, 2016; final manuscript received March 14, 2017; published online May 3, 2017. Assoc. Editor: Marc Horner.

rotor speed and decreases rotor torque for a given pump-operating condition. The hydraulic performance of the pump is also affected by the secondary flow clearances, which are fluid films between the impeller and casing through which blood can recirculate around the pump to prevent stagnation.

Hemolysis is caused by a combination of high shear stress and exposure time. These quantities are influenced by blade geometry, surface roughness, and clearance geometry. In this paper, we vary blade geometry and consider the surface roughness and clearance geometry to be fixed. While hemolysis can occur on the pump blades, where high shear can be observed, most hemolysis in contactless centrifugal pumps occurs in the secondary flow clearances where exposure time is far higher [17]. In this paper, the rotor speed is adjusted for each blade geometry until the operating condition is met. For a fixed operating condition and fixed secondary flow clearance geometry, we assume that the hemolysis is primarily affected in this case by the rotor speed of the device, and the so increased rotor speed is used as an indicator of increased hemolysis in this paper. Although Eulerean and Lagrangian methods are available to calculate a measure of hemolysis from shear stress and exposure time [18], the computational cost of these methods for the large number of designs given in this paper is beyond the scope of this work.

The methodology described here requires definition of a fixed hub and rim diameter and blade thickness, and then, uses an analytical code to define the machinable blade curvature angles for a given number of blades. CFD analysis is used to create a response surface for each number of blades. For a given number of blades, the outlet width and blade angle for the two different impellers which exhibit maximum efficiency and minimum rotor speed are then determined.

3 Machinability

The analytical scheme assumes a centrifugal impeller with blade geometry composed of N equiangular spirals of constant angle b and a blade thickness t. The impeller has a hub radius R_{in} and rim radius R_{out}. The impeller is viewed in polar coordinates, with 0 deg equidistant between two leading edges (LEs), as shown in Fig. 1.

The angular position θ of an equiangular spiral at radial coordinate r is given by

$$\theta(r) = \frac{1}{\cot(b)} \ln(r/a)$$

The quantity a is given a value of 1 mm in this paper. The blade angular span at the hub, ρ, and the angular separation between blades, δ, are given by

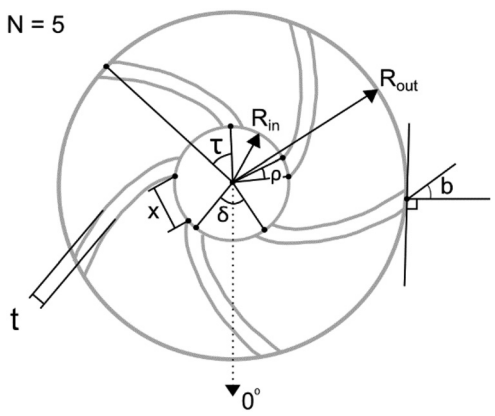

Fig. 1 Impeller geometry composed of *N* equiangular blades with thickness *t* and constant angle *b*, and inner and outer radii R_{in} and R_{out}

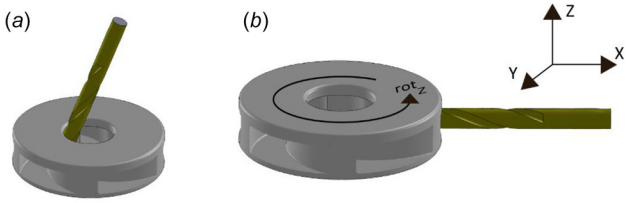

Fig. 2 (*a*) Cutting from inside the hub to clean up the leading edge geometry, and (*b*) cutting in from the outer radius with three translational axes and one rotational

$$\rho = 2 \cdot \sin^{-1}\left(\frac{\frac{t}{2}}{R_{in}}\right)$$

$$\delta = {}^{2\pi}/_{N}$$

The angular travel of each blade, τ, can be found by subtracting the angular position at the rim from the angular position at the base

$$\tau = \theta(R_{out}) - \theta(R_{in})$$

A ball-nosed cutter with a known diameter (d_{cut}) would be used to machine the cavities out of a block of material to create the blade geometry. We assume that this cutter can pass through the hub from above the shroud to clean up the leading edge geometry (Fig. 2(*a*)), but the blade shapes are formed by cutting in from the outer radius (Fig. 2(*b*)). We assume that when cutting in from the outer radius, the cutter is free to move in X, Y, and Z directions, and the impeller can be rotated on its axis.

Our methodology states that a two-dimensional impeller geometry is machinable by this method if it satisfies three conditions:

(1) The cutter must be smaller than the gap between leading edges.
(2) The cutter must be able to manufacture the leading edge suction side.
(3) The cutter must be able to manufacture the leading edge pressure side.

3.1 Condition 1. The first condition is that the cutter must be able to pass through the gap between the blades at the inner hub, x. The chord x is calculated using the following formula:

$$x = 2 \cdot R_{in} \cdot \sin\left(\frac{\delta - \rho}{2}\right)$$

$$\text{Condition 1}: \ (x > d_{Cut})$$

where d_{cut} is the diameter of the cutter.

3.2 Condition 2. The second condition is that the cutter must be able to machine the suction side of the leading edge. A large angular travel in the blades or a large number of blades can prevent the cutter from being able to access the leading edge (LE) from the outer radius without damaging the subsequent leading edge (LE′). This is shown in Fig. 3 for a series of five-bladed impellers with increasing blade angle. The geometry was defined by $N = 5$, $R_{in} = 6$ mm, $R_{out} = 15$ mm, $t = 2$ mm, and $d_{cut} = 2$ mm.

Condition 2 states that the minimum angle at which the cutter passes the trailing edge (TE) to reach LE (θ_{TE-LE}, Fig. 4(*b*)) must be less than the maximum angle at which the cutter passes the LE′ to reach the leading edge ($\theta_{LE'-LE}$, Fig. 4(*c*)). If this condition ($\theta_{TE-LE} < \theta_{LE'-LE}$) is not met, then, the cutter cannot machine the LE, and the impeller is not machinable.

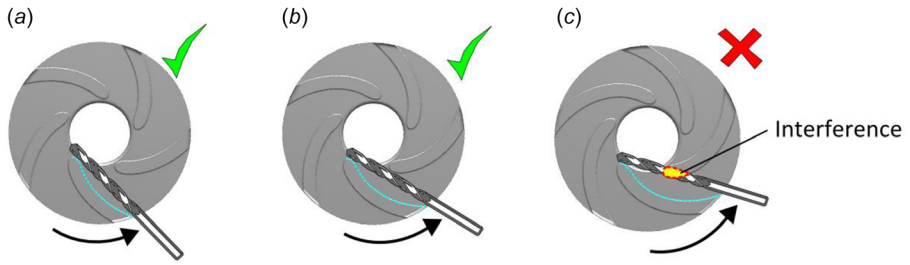

Fig. 3 Increasing the blade angle until the cutter can no longer reach the LE suction side. (*a*) 50 deg and (*b*) 55 deg are machinable, and (*c*) 60 deg is not.

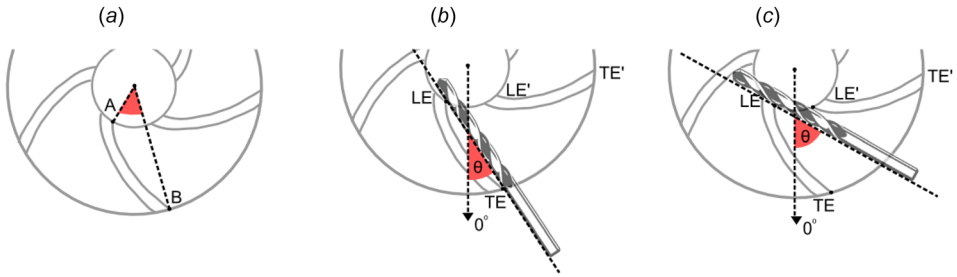

Fig. 4 (*a*) θ_{A-B}, the angle between the LE and TE points on the blade's suction side, (*b*) θ_{TE-LE}, where the cutter is in contact with LE and TE, and (*c*) $\theta_{LE-LE'}$, where the cutter is in contact with LE and LE′

Table 1 Evaluation of condition 2 for the three five-bladed impellers shown in Fig. 3

Angle	50	55	60
θ_{TE-LE}	49.8	62.5	77.3
$\theta_{LE'-LE}$	68.0	68.0	68.0
Condition 2 ($\theta_{TE-LE} < \theta_{LE'-LE}$)	True	True	False

The angular separation between the points A and B, θ_{A-B}, is defined as $\tau - \rho/2 + \rho_{out}/2$, where ρ_{out} is the angular width of the blade at the outer rim. θ_{TE-LE} and $\theta_{LE'-LE}$ are calculated using the following derived equations:

$$\theta_{TE-LE} = \tan^{-1}\left(\frac{R_{in} \cdot \sin(\theta_{A-B})}{R_{out} - R_{in} \cdot \cos(\theta_{A-B})}\right) + \tau - \frac{\delta}{2}$$

$$\theta_{LE'-LE} = \cos^{-1}\left(\frac{d_{cut}}{x}\right)$$

$$\text{Condition 2: } \theta_{TE-LE} < \theta_{LE'-LE}$$

These angles were calculated for the three impellers shown in Fig. 3. The results indicate whether the leading edge suction side is machinable and are shown in Table 1.

3.3 Condition 3. The third condition is that the cutter must be able to machine the pressure side of the leading edge. A large angular travel in the blades or a large number of blades can prevent the cutter from being able to access this area from the outer radius. This is shown in Fig. 5 for a series of five-bladed impellers with increasing blade angle. The geometry was defined by $N = 5$, $R_{in} = 6$ mm, $R_{out} = 15$ mm, $t = 2$ mm, and $d_{cut} = 2$ mm.

Condition 3 states that the minimum angle at which the cutter passes TE ($\theta_{TE-LE'}$) to reach the LE′ (Fig. 6(*b*)) must be less than the tangential angle of the curvature at the LE′ suction side ($\theta_{LE'-TAN}$, Fig. 6(*c*)). If the condition ($\theta_{LE'-TAN} > \theta_{TE-LE'}$) is not met, then, the cutter cannot create the correct geometry at the LE suction side, and the impeller is not machinable.

The angular separation between the points C and D, θ_{C-D}, is defined as $\tau - \delta - \theta_{CUT}$, where θ_{CUT} is the angular width of the cutter at the hub, approximated as $\theta_{CUT} = d_{Cut}/R_{in}$. $\theta_{TE-LE'}$ and $\theta_{LE'-TAN}$ are calculated using the following equations:

$$\theta_{TE-LE'} = \tan^{-1}\left(\frac{R_{in} \cdot \sin(\theta_{C-D})}{R_{out} - R_{in} \cdot \cos(\theta_{C-D})}\right) + \tau - \frac{\delta}{2}$$

$$\theta_{LE'-TAN} = b + \frac{\pi}{N}$$

$$\text{Condition 3: } \theta_{TE-LE'} < \theta_{LE'-TAN}$$

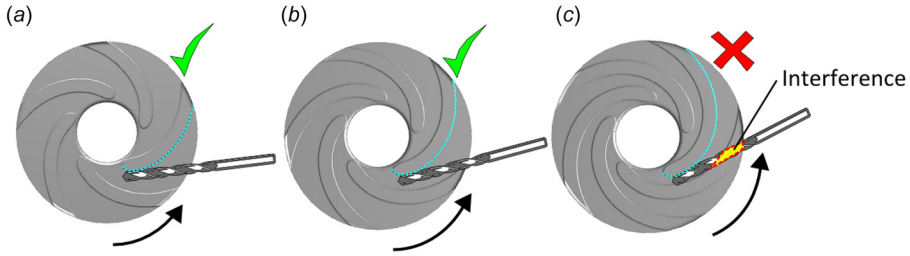

Fig. 5 Increasing the blade angle until the cutter can no longer reach the LE pressure side. The pressure side of (*a*) 60 deg and (*b*) 65 deg are machinable, and (*c*) 70 deg is not.

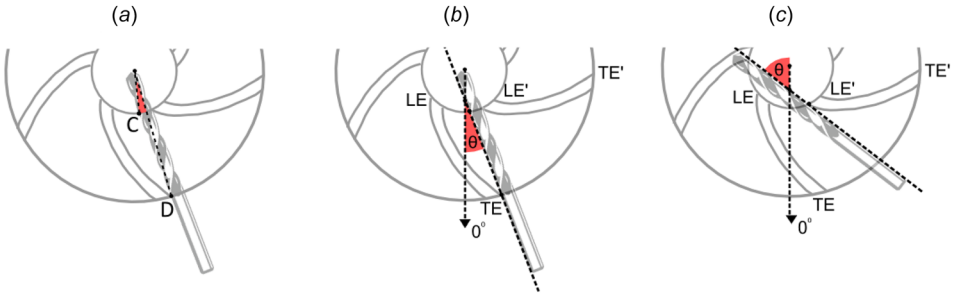

Fig. 6 (*a*) θ_{C-D}, the angle between the points where the clockwise edge of the cutter meets the rim and hub, (*b*) $\theta_{TE-LE'}$, the minimum angle at which the cutter passes the TE to manufacture the suction side of LE′, and (*c*) $\theta_{LE'-TAN}$, the angle required to machine the geometry at the suction side of LE′

Table 2 Evaluation of condition 3 for the three five-bladed impellers shown in Fig. 5

Angle	60	65	70
$\theta_{TE-LE'}$	54.8	89.7	131.1
$\theta_{LE'-TAN}$	96.0	101.0	106.0
Condition 3	True	True	False

These angles were calculated for the three impellers shown in Fig. 5. The results, shown in Table 2, indicate whether the leading edge pressure side is machinable.

3.4 Analytical Results. If all the three conditions are satisfied, we can denote an impeller design as machinable. A MATLAB code was used to iteratively determine the maximum machinable constant angle, b, for a given impeller with known R_{in}, R_{out}, t, and N. For our case, we fixed d_{cut}, t, R_{in} and R_{out}, and varied N from 3 to 9. We used $R_{in} = 6$ mm, $R_{out} = 15$ mm, $t = 2$ mm, and $d_{cut} = 2$ mm. The analytical code gave the results shown in Table 3.

Impellers with 8 and 9 blades with the described geometry had no access for the cutter into the hub. For the rest of the impellers, the maximum machinable angle decreases as the number of blades increases, and cutter access to the hub becomes more limited. In all cases, the manufacture was limited by condition 1 or 2.

4 Computational Fluid Dynamics

ANSYS CFX was used to analyze the machinable impeller geometries. The blood is modeled as incompressible fluid with a viscosity of 3.5 mPa·s and a density of 1050 kg/m^3. Because of the high shear rate inside rotary blood pumps (>100 s^{-1}), the blood is treated as Newtonian [19]. Three-dimensional cases with three to seven blades were simulated. The depth of the blades, hereafter referred to as tip width, was constrained between 3 mm and 5.8 mm. The volute had a height of 6 mm, the secondary flow clearances were 0.25 mm, and the volute tongue was 0.6 mm from the outer edge of the impeller blades. A steady-state, frozen rotor

Table 3 Maximum machinable constant angle b for impellers with three to nine blades with $R_{in} = 6$ mm, $R_{out} = 15$ mm, $t = 2$ mm, and $d_{cut} = 2$ mm

Blades, N	3	4	5		
Angle, b_{max}	65	58	52		
Condition	2	2	2		
Impeller	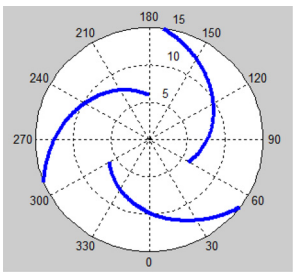	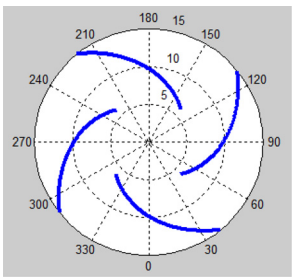	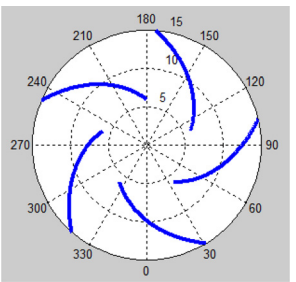		
Blades, N	6	7	8	9	
Angle, b_{max}	44	32	—	—	
Condition	2	2	1	1	
Impeller	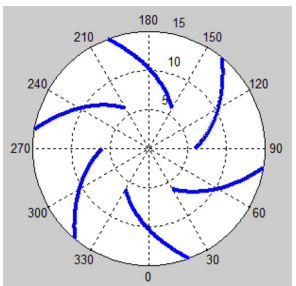	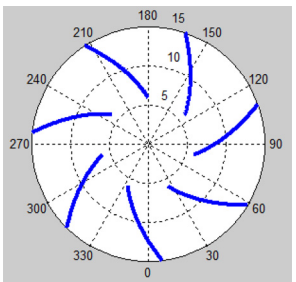	—	—	

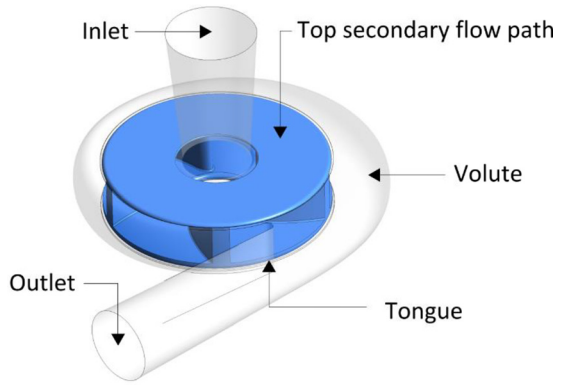

Fig. 7 The model used in the CFD analysis

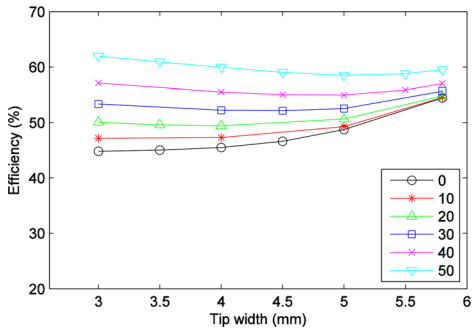

Fig. 9 The effect of tip width on efficiency for a five-bladed impeller for all machinable blade angles

model was used. The CFD model included the pump, an inlet, a volute, and secondary flow clearances as shown in Fig. 7.

For each case, a response surface was created using the ANSYS response surface tool. Each response surface is formed by solving 15 individual cases in which three variables of outlet angle, blade tip width, and rotor speed vary within a certain range, using the ANSYS design of experiment tool. For each number of blades, the blade angle is varied from 0 to the maximum machinable angle, and the rotor speed is varied to the required speed to generate the target operating condition. The target operating condition is a static pressure rise of 100 mmHg and a flow rate of 5 L/min, similar to the conditions used by other researchers [20]. The applied boundary conditions were an average inlet static pressure of 0 Pa, an outlet flow rate of 5 L/min, and a no-slip wall condition. From each response surface, the combination of optimized blade angle and outlet widths, exhibiting the lowest rotor speed and highest efficiency for the target operating condition were found. From these results, we were able to show the effect of these blade number and angle on rotor speed and efficiency.

Tetrahedral elements with prism elements to form inflation layers along the wetted surfaces were used for meshing. A five-layer structure was used with a growth rate of 1.2 and a transition ratio of 0.75. The $Y+$ values were between 13 and 17 for all cases which falls within the desired range for the k/ε turbulence model with scalable wall functions used in this study. A mesh sensitivity study was performed on our pump model in which the number of elements was increased until the output pressure was stable. We observed minimal change in the output pressure beyond 800,000 elements. Our simulations each used >1,100,000 elements.

The speed and efficiency of the impellers with tip width optimized for highest efficiency are shown in Fig. 8.

The efficiency increases as blade angle increases. For a given blade angle, an increase in the number of blades resulted in a higher efficiency up until six blades, although seven blades showed no clear improvement from 6. The rotor speed was higher with fewer blades but was minimally affected by blade angle. The maximum efficiency with machinable geometries occurred with three blades at the maximum machinable angle of 65. The tip width that provided maximum efficiency was 5.8 mm in all cases with six- and seven-bladed impellers. With three to five blades, the tip width that offered maximum efficiency was dependent on the blade angle. This causes the sharp rise in the rotor speed observable in the three-, four-, and five-bladed impellers at angles of 10 deg, 40 deg, and 40 deg, respectively.

For a five-bladed impeller, the tip width that provides maximum efficiency changes from 5.8 to 3 mm between 40 deg and 50 deg blade angles as shown in Fig. 9. The same graph for the six-bladed impeller is shown in Fig. 10.

The speed and efficiency of the impellers with tip width optimized for lowest speed are shown in Fig. 11.

The required rotor speed increases very slightly as blade angle increases. For a given blade angle, an increase in the number of blades resulted in a lower speed up until six blades, although seven blades showed no clear improvement from six. The efficiency at a given angle was higher with more blades and tended to increase as the blade angle increased. The minimum speed with a machinable geometry occurred with the seven-bladed geometry at a blade angle of 0 deg. For all cases, the tip width that provided the lowest rotor speed was the maximum, 5.8 mm, as shown for a five-bladed impeller in Fig. 12.

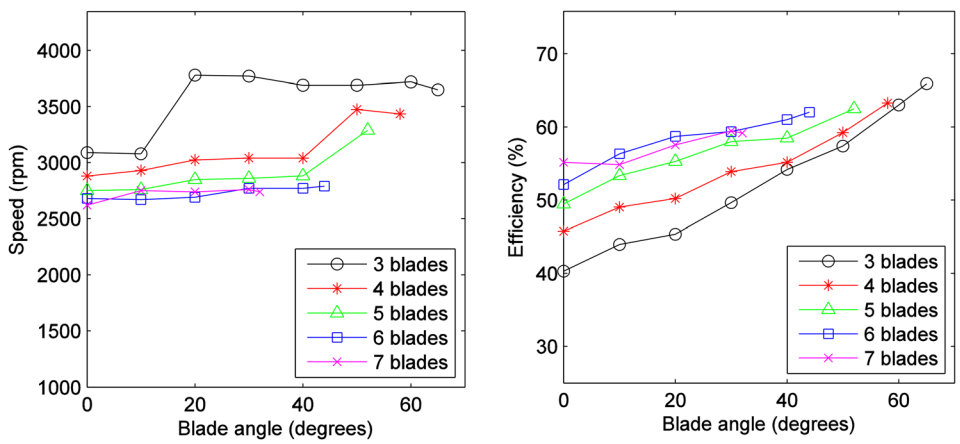

Fig. 8 The results for impellers with tip width optimized for maximum efficiency: left, rotor speed; right, efficiency

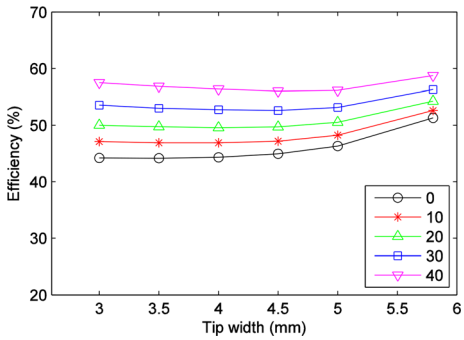

Fig. 10 The effect of tip width on efficiency for a six-bladed impeller for all machinable blade angles

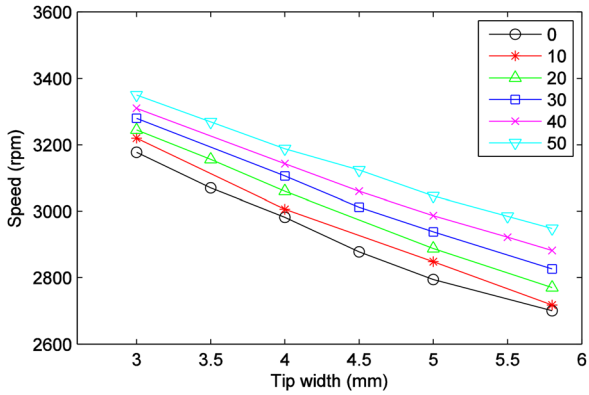

Fig. 12 The effect of tip width on rotor speed for a five-bladed impeller and all machinable blade angles

5 Discussion

5.1 Analysis. The maximum machinable blade angle decreases as the number of blades increases. For our geometry, the maximum machinable number of blades was seven, although this will vary depending on the preset geometry. Condition 3 was not the limiting factor for any geometry we tested, and this may be true for all equiangular spirals although not necessarily for blades with nonconstant angles.

The CFD results show the contrast between the competing aims of reducing pump speed and increasing efficiency. Increasing the blade angle will increase the efficiency. However, a higher blade angle will also reduce the torque and increase the required rotor speed, resulting in higher shear stress and consequently more hemolysis in secondary flow paths. From our analysis, we find that for the geometry used in this case study, a six- or seven-bladed impeller with a low blade angle results in the lowest speed and highest efficiency despite the manufacturing limitations on such an impeller. This will vary depending on the predefined inner and outer radii, thickness, and tip width limits.

The results also suggest that, for our geometry, there is a limit to improvements in efficiency and reductions in rotor speed as the blade number is increased beyond six. This is likely due to the increased blade surface area and consequently increased skin friction. The CFD analysis would have to be applied to nonmachinable impellers with higher blade numbers to validate this observation, but this is outside of the scope of this paper.

5.2 Limitations. There are limitations with both the analytical and CFD methods used in this paper, which are discussed here. The analytical code made some assumptions in order to simplify analysis. Equiangular spirals are not necessarily the most efficient blade shape for a given geometry. It also assumes an unlimited cutter length, and a simplified leading edge geometry based on the fact that the leading edge can be cleaned up from the hub. These assumptions were necessary to create a simple analytical framework for impeller machinability assessment. Machinability can be assessed on a case-by-case basis more accurately, but an analytical solution provides a method that can be integrated with optimization and provides fast results for a given geometry. The machinability constraint means that there are potentially more optimal designs that have not been simulated; however, it gives necessary focus to the paper.

In this study, the rotor speed has been used as an indicator for the hemolysis in secondary flow clearances, on the assumption that hemolysis is directly related to rotor speed for a given operating condition. However, hemolysis is described in several recent models as a function of the shear stress and the residence time of red blood cells [21]. Higher rotor speed leads to a higher shear stress within the secondary flow clearances which will contribute to hemolysis. The extent of the resulting hemolysis will be dependent on the exposure time of the blood. In our future study, we will use an empirical model of hemolysis as described by Giersierpen et al. [22]. This model has been used by many investigators in this field [18]. Experimental hemolysis validation would also give greater weight to this analysis.

We used Ansys' automatic mesh tool to form the response surface. The automatic Ansys mesh tool is beneficial for the optimization process as each subsequent case with a change in the geometry will be meshed automatically based on the input for the initial case. Although this technique makes the process quicker, it gives us less control on the mesh quality for different geometries. Consequently, a number of mesh complications such as mesh

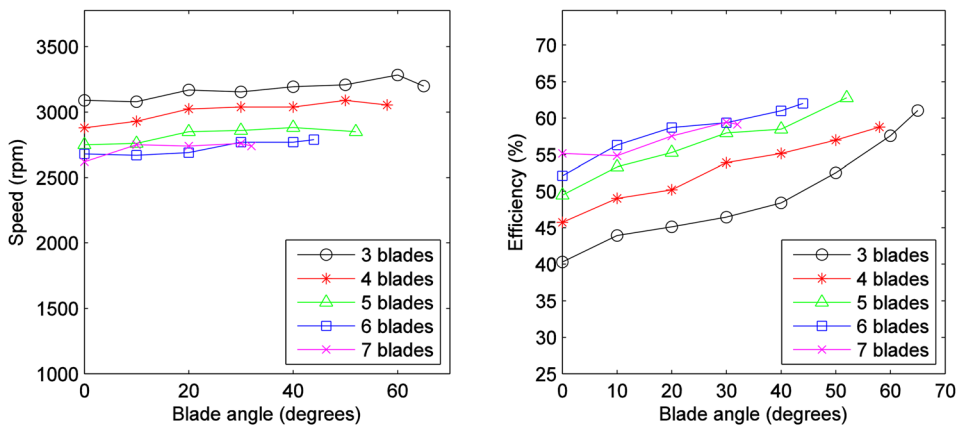

Fig. 11 The results for impellers with tip width optimized for minimum rotor speed: left, rotor speed; right, efficiency

skewness and high aspect ratio which may have an effect on the final results will be ignored. This is a necessary limitation for the high number of cases in this study. For the same reason, a k–ε turbulence model was used instead of the shear stress transport turbulence model, which is generally thought to be more accurate in terms of shear stress [23]. We also note that this assessment does not take into account impeller stability [24,25] or changing conditions, operating conditions, within the pump [25,26], and it is possible that the off-design performance deviates from the observed steady-state performance at the nominal, 5 L/min flow condition studied.

6 Conclusion

The analytical code presented in this paper can be used to quickly define limits on machinable geometry for shrouded equiangular spiral blades for a given impeller size and blade thickness. This method was used in a case study to provide a set of constraints on machinable geometries for three to nine blades. The machinable set were then created in CFD and analyzed at an operating condition of 5 L/min and 100 mmHg. This analysis provided useful information on the machinable geometries for our case study, and showed that in this case, six or seven blades and a low blade angle provided the optimal performance. Although these results apply only to our case study, the methodology described here can be used for any predefined geometry. Our group aims to use the same methodology for a more detailed CFD analysis of hemolysis both on the pump blades and in secondary flow clearances.

Acknowledgment

This report is an independent research funded by the National Institute for Health Research (Investment for innovation (i4i), Turbocardia, Grant No. II-LB-1111-20007). Principal Investigator for the grant is Professor T. Korakianitis. The views expressed in this publication are those of the authors and not necessarily those of the NHS, the National Institute for Health Research or the Department of Health.

References

[1] Lloyd, J., 2011, "Heart Disease and Stroke Statistics—2009 Update: A Report From the American Heart Association Statistics Committee and Stroke Statistics Subcommittee," Circulation, **124**(16), p. 424.
[2] Griffith, B., Kormos, R., Borovetz, H., Litwak, K., Antaki, J., Poirier, V., and Butler, K., 2001, "HeartMate II Left Ventricular Assist System: From Concept to First Clinical Use," Ann. Thorac. Surg., **71**(3), pp. S116–S120.
[3] Christiansen, C., Klocke, A., and Autschbach, R., 2008, "Past, Present, and Future of Long-Term Mechanical Cardiac Support in Adults," J. Card. Surg., **23**(6), pp. 664–676.
[4] Bourque, K., Gernes, D. B., Loree, H. M., Richardson, J. S., Poirier, V. L., Barletta, N., Fleischli, A., Foiera, G., Gempp, T. M., and Schoeb, R., 2001, "HeartMate III: Pump Design for a Centrifugal LVAD With a Magnetically Levitated Rotor," ASAIO J., **47**(4), pp. 401–405.
[5] Wood, C., Maiorana, A., Larbalestier, R., Lovett, M., Green, G., and O'Driscoll, G., 2008, "First Successful Bridge to Myocardial Recovery With a HeartWare HVAD," J. Heart Lung Transplant., **27**(6), pp. 695–697.
[6] Hoshi, H., Shinshi, T., and Takatani, S., 2006, "Third-Generation Blood Pumps With Mechanical Noncontact Magnetic Bearings," Artif. Organs, **30**(5), pp. 324–338.
[7] Yamazaki, K., Kihara, S., Akimoto, T., Tagusari, O., Kawai, A., and Umezu, M., 2007, "EVAHEART™: An Implantable Centrifugal Blood Pump for Long-Term Circulatory Support," Jpn. J. Thorac. Cardiovasc. Surg., **50**(11), pp. 461–465.
[8] Molteni, A., Fraser, K., Yousef, H., Low, K., Rolland, S., and Foster, G., 2014, "Development, Validation and Use of a CFD Model for Iterative Design Improvement of the Calon MiniVAD," Int. J. Artif. Organs, **37**(8), pp. 586–587.
[9] Fan, Y., Tansley, G., Fan, H., and Niu, J., 2011, "The Application of Laser Welding on Left Ventricular Assist Device (LVAD)," Symposium on Photonics and Optoelectronics (SOPO), Wuhan, China, May 16–18.
[10] Olin, C., 2001, "Titanium in Cardiac and Cardiovascular Applications," *Titanium in Medicine*, Springer, Heidelberg, p. 889.
[11] Taskin, M., Zhang, T., Fraser, K., Griffith, B., and Wu, J., 2012, "Design Optimization of a Wearable Artificial Pump-Lung Device With Computational Modeling," ASME J. Med. Devices, **6**(3), p. 031009.
[12] Wu, J. Z., Antaki, J., Verkaik, J., Snyder, S., and Ricci, M., 2012, "Computational Fluid Dynamics-Based Design Optimization for an Implantable Miniature Maglev Pediatric Ventricular Assist Device," ASME J. Fluids Eng., **134**(4), p. 041101.
[13] Korakianitis, T., Rezaienia, M. A., Paul, G., Rahideh, A., Rothman, M., and Mozafari, S., 2016, "Optimization of Centrifugal Pump Characteristic Dimensions for Mechanical Circulatory Support Devices," ASAIO J., **62**(5), pp. 545–551.
[14] Mozafari, S., Rezaienia, M. A., Paul, G., Rothman, M., Wen, P., and Korakianitis, T., 2016, "The Effect of Geometry on the Efficiency and Hemolysis of Centrifugal Implantable Blood Pumps," ASAIO J., **63**(1), pp. 53–59.
[15] Korakianitis, T., Rezaienia, M., Hamakhan, I., and Wheeler, P., 2013, "Two- and Three-Dimensional Prescribed Surface Curvature Distribution Blade Design (CIRCLE) Method for the Design of High Efficiency Turbines, Compressors, and Isolated Airfoils," ASME J. Turbomach., **135**(4), p. 041002.
[16] Shen, X., Avital, E., Rezaienia, M. A., Paul, G., and Korakianitis, T., 2006, "Computational Methods for Investigation of Surface Curvature Effects on Airfoil Boundary Layer Behavior," J. Algorithms Comput. Technol., **11**(1), pp. 68–82.
[17] Taskin, M. E., Fraser, K. H., Zhang, T., Gellman, B., Fleischli, A., Dasse, K. A., Griffith, B. P., and Wu, Z. J., 2010, "Computational Characterization of Flow and Hemolytic Performance of the UltraMag Blood Pump for Circulatory Support," Artif. Organs, **34**(12), pp. 1099–1113.
[18] Taskin, M. E., Fraser, K. H., Zhang, T., Wu, C., Griffith, B. P., and Wu, Z. J., 2012, "Evaluation of Eulerian and Lagrangian Models for Hemolysis Estimation," ASAIO J., **58**(4), pp. 363–372.
[19] Fraser, K., Zhang, T., Taskin, M., Griffith, B., and Wu, Z. J., 2012, "A Quantitative Comparison of Mechanical Blood Damage Parameters in Rotary Ventricular Assist Devices: Shear Stress, Exposure Time and Hemolysis Index," ASME J. Biomech. Eng., **134**(8), p. 081002.
[20] Ishii, K., Hosoda, K., Isoyama, T., Saito, I., Ariyoshi, K., Inoue, Y., Sato, M., Hara, S., Lee, X., Wu, S. Y., and Ono, T., 2013, "Pulsatile Driving of the Helical Flow Pump," 35th Annual International Conference of the IEEE Engineering in Medicine and Biology Society (EMBC), Osaka, Japan, July 3–7, pp. 2724–2727.
[21] Fraser, K. H., Taskin, M. E., Griffith, B. P., and Wu, Z. J., 2011, "The Use of Computational Fluid Dynamics in the Development of Ventricular Assist Devices," Med. Eng. Phys., **33**(3), pp. 263–280.
[22] Giersiepen, M., Wurzinger, L. J., Opitz, R., and Reul, H., 1990, "Estimation of Shear Stress-Related Blood Damage in Heart Valve Prostheses—In Vitro Comparison of 25 Aortic Valves," Int. J. Artif. Organs, **13**(5), pp. 300–306.
[23] Thamsen, B., Blümel, B., Schaller, J., Paschereit, C. O., Affeld, K., Goubergrits, L., and Kertzscher, U., 2015, "Numerical Analysis of Blood Damage Potential of the HeartMate II and HeartWare HVAD Rotary Blood Pumps," Artif. Organs, **39**(8), pp. 651–659.
[24] Paul, G., Rezaienia, M. A., Rahideh, A., Munjiza, A., and Korakianitis, T., 2016, "The Effects of Ambulatory Accelerations on the Stability of a Magnetically Suspended Impeller for an Implantable Blood Pump," Artif. Organs, **40**(9), pp. 867–876.
[25] Timms, D., Hayne, M., Tan, A., and Pearcy, M., 2005, "Evaluation of Left Ventricular Assist Device Performance and Hydraulic Force in a Complete Mock Circulation Loop," Artif. Organs, **29**(7), pp. 573–580.
[26] Rezaienia, M. A., Paul, G., Avital, E., Rahideh, A., Rothman, M., and Korakianitis, T., 2016, "In-Vitro Investigation of Cerebral-Perfusion Effects of a Rotary Blood Pump Installed in the Descending Aorta," J. Biomech., **49**(9), pp. 1865–1872.